VIP Zinc Batteries Very Important Paper

How to cite:
International Edition: doi.org/10.1002/anie.202107378
German Edition: doi.org/10.1002/ange.202107378

Highly Reversible Aqueous Zinc Batteries enabled by Zincophilic–Zincophobic Interfacial Layers and Interrupted Hydrogen-Bond Electrolytes

Longsheng Cao[+], Dan Li[+], Fernando A. Soto[+], Victor Ponce, Bao Zhang, Lu Ma, Tao Deng, Jorge M. Seminario, Enyuan Hu, Xiao-Qing Yang, Perla B. Balbuena, and Chunsheng Wang**

Abstract: *Aqueous Zn batteries promise high energy density but suffer from Zn dendritic growth and poor low-temperature performance. Here, we overcome both challenges by using an eutectic 7.6 m $ZnCl_2$ aqueous electrolyte with 0.05 m $SnCl_2$ additive, which in situ forms a zincophilic/zincophobic Sn/$Zn_5(OH)_8Cl_2{\cdot}H_2O$ bilayer interphase and enables low temperature operation. Zincophilic Sn decreases Zn plating/stripping overpotential and promotes uniform Zn plating, while zincophobic $Zn_5(OH)_8Cl_2{\cdot}H_2O$ top-layer suppresses Zn dendrite growth. The eutectic electrolyte has a high ionic conductivity of ≈0.8 mS cm^{-1} even at −70 °C due to the distortion of hydrogen bond network by solvated Zn^{2+} and Cl^-. The eutectic electrolyte enables Zn || Ti half-cell a high Coulombic efficiency (CE) of >99.7 % for 200 cycles and Zn || Zn cell steady charge/discharge for 500 h with a low overpotential of 8 mV at 3 mA cm^{-2}. Practically, Zn || $VOPO_4$ batteries maintain >95 % capacity with a CE of >99.9 % for 200 cycles at −50 °C, and retain ≈30 % capacity at −70 °C of that at 20 °C.*

Introduction

Aqueous Zn batteries are promising for grid-energy storage due to the abundance, high theoretical capacity (820 mAh g^{-1} and 5851 mAh cm^{-3}), and water compatibility of Zn anodes.[1] However, the lifetime of Zn batteries is challenged by low Coulombic efficiency (CE) of Zn plating/stripping, due to water consumption and Zn dendrite growth. Besides, the bulk aqueous electrolytes suffer from high freezing-temperature of water, limiting low-temperature performance of aqueous Zn batteries. Recently, the freezing temperature of aqueous electrolytes is reduced to −70 °C by molecular-level design.[2] Then the design of solid electrolyte interphase (SEI) to suppress Zn dendrite and enhance the CE becomes critical for high performance aqueous Zn batteries.

Parasitic water reduction on Zn surface during Zn deposition is accelerated by the strong Coulombic interactions between solvated Zn^{2+} and its surrounding H_2O shell. The local pH increase due to hydrogen evolution promotes the formation of Zn^{2+}-insulating passivate layer on Zn, reducing Zn^{2+} transport kinetics, inducing Zn dendrite growth and continuous water consumption. Formation of a Zn^{2+} conductive zincophobic SEI on Zn surface can effectively suppress water reduction and Zn dendrite growth. The SEI can be designed by reducing the thermodynamic reactivity of water and decomposition of aqueous electrolytes. To reduce water activity, Ji's group[3] designed a 30 m $ZnCl_2$-5 m LiCl water-in-bisalt (WIBS) electrolyte, where the hydrogen bond network of water is interrupted and Zn^{2+} are closely coordinated with Cl^- rather than H_2O, thus strengthening O-H covalent bonds. $ZnCl_2$ is one of the most soluble inorganic salts[4] and can reduce H-bonds in water by increasing salt concentration. Chen et al.[2] reported a 7.5 m $ZnCl_2$ electrolyte with interrupted hydrogen bond network of water allowing Zn plating/stripping even at −70 °C. However, how bulk electrolyte property affects SEI formation on Zn anode surface was still unexplored.

To promote the in situ SEI formation, salts, organic solvents or additives with a higher reduction potential than Zn plating, were introduced in aqueous Zn batteries to reduce water activity and water number in Zn^{2+} solvation shell.[5] However, it is challenging to in situ form SEI that has high Zn^{2+} conductivity, low electronic conductivity, and high zincophobicity to achieve a high CE and fast reaction kinetics even at a low-temperature. Although artificial interphase,

[*] Dr. L. Cao,[+] Dr. D. Li,[+] Dr. B. Zhang, Dr. T. Deng, Prof. C. Wang
Department of Chemical and Biomolecular Engineering, University of Maryland
College Park, MD 20742 (USA)
E-mail: cswang@umd.edu

Dr. F. A. Soto,[+] Dr. V. Ponce, Dr. J. M. Seminario, Prof. P. B. Balbuena
Department of Chemical Engineering, Texas A&M University
College Station, TX 77843 (USA)
E-mail: balbuena@tamu.edu

Dr. L. Ma
National Synchrotron Light Source II, Brookhaven National Laboratory
Upton, NY 11973 (USA)

Dr. J. M. Seminario, Prof. P. B. Balbuena
Department of Materials Science and Engineering, Texas A&M University
College Station, TX 77843 (USA)

Dr. E. Hu, Dr. X. Yang
Chemistry Division, Brookhaven National Laboratory
Upton, NY 11973 (USA)

Dr. J. M. Seminario
Department of Electrical and Computer Engineering, Texas A&M University
College Station, TX 77843 (USA)

[+] These authors contributed equally to this work.

Supporting information and the ORCID identification number(s) for the author(s) of this article can be found under: https://doi.org/10.1002/anie.202107378.

including $CaCO_3$,[6] polyamide,[7] tin[8] and graphene[9] coating layers, can suppress water decomposition, they lack self-repairability and gradually loss the functions. To achieve high performance in a wide temperature range, aqueous electrolytes should be able to in situ form a zincophilic layer on current collector for uniform Zn plating, and a dense zincophobic SEI to suppress water decomposition and Zn dendrite growth, with broken water hydrogen network even at low temperature.

Here, we introduced 0.05 m $SnCl_2$ additive into eutectic 7.6 m $ZnCl_2$ aqueous electrolyte[10] (denoted as 7.6 m $ZnCl_2$-0.05 m $SnCl_2$) to form a zincophilic Sn layer on current collector for uniform Zn plating, and a dense zincophobic $Zn_5(OH)_8Cl_2{\cdot}H_2O$ SEI to suppress water decomposition and Zn dendrite growth. A high CE of Zn plating/stripping in a wide temperature window from +20 to −70 °C was achieved in 7.6 m $ZnCl_2$-0.05 m $SnCl_2$. As in Figure 1, such an aqueous

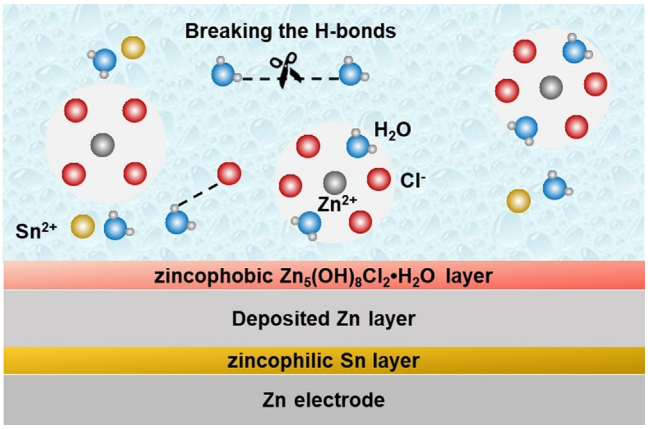

Figure 1. Scheme of electrolyte and electrolyte–electrode-interphase structure.

electrolyte has multiple advantages: (1) The eutectic 7.6 m $ZnCl_2$ balanced the charge carrier density and mobility enabling high Zn^{2+} conductivity at a low temperature. (2) The replacement of H_2O in Zn^{2+} solvation sheath by concentrated Cl^- and strong H_2O-Cl^- interactions decreased water activity. (3) The in situ formed zincophilic Sn on substrate tightly anchors Zn foil, and facilitates the formation of a uniform zincophobic $Zn_5(OH)_8Cl_2{\cdot}H_2O$ SEI, suppressing Zn dendrite growth and water decomposition. The combination of reduced water activity and zincophilic-zincophobic interfacial bilayer enable dendrite-free Zn plating/stripping to achieve a high CE of 99.7 % for > 500 h. The eutectic 7.6 m $ZnCl_2$-0.05 m $SnCl_2$ electrolyte enables Zn || $VOPO_4$ full cells at −70 °C to achieve a 30 % of capacity at 20 °C and > 95 % of capacity retention after 200 cycles at −50 °C.

Results and Discussion

Solvation structure and property of $ZnCl_2$ electrolytes

The electrochemical stability windows at room-temperature and the ionic conductivity of aqueous electrolytes at

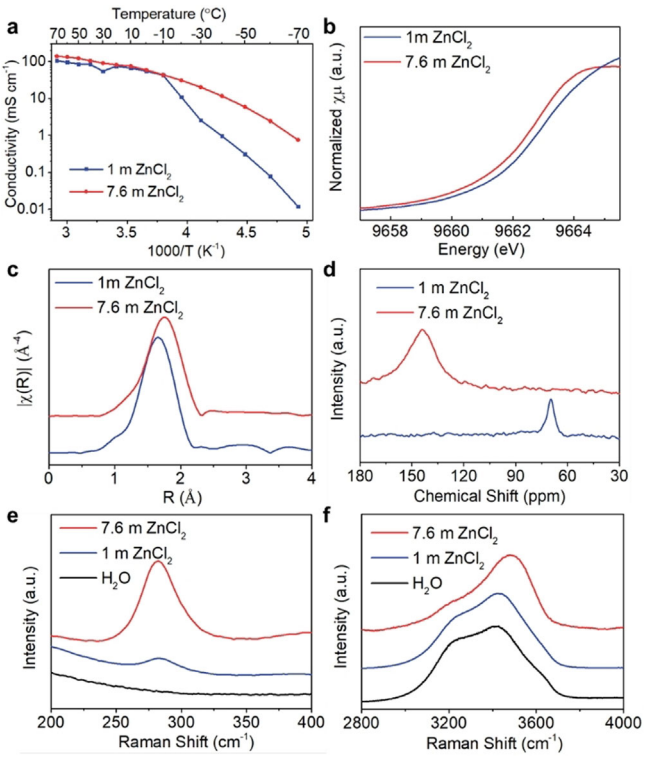

Figure 2. Physical properties and structure of $ZnCl_2$ aqueous electrolytes. a) Ionic conductivity at different temperatures. b) X-ray absorption near edge structure (XANES) and c) Fourier transformed extended X-ray absorption fine structure (ft-EXAFS) spectra of 1 m and 7.6 m $ZnCl_2$ aqueous electrolytes. d) The ^{67}Zn nuclear magnetic resonance (NMR) spectra and e) Raman spectra between 150 and 500 cm^{-1} of electrolytes. The bands at around 230 cm^{-1} are related to $[ZnCl_4]^{2-}$. The bands at around 290 cm^{-1} are related to $[Zn(OH_2)_2Cl_4]^{2-}$. The bands at around 312 cm^{-1} are related to polymeric species. The bands at around 390 cm^{-1} are related to $[Zn(OH_2)_6]^{2+}$.[12] f) The Raman spectra of OH stretching bands between 2800 and 4000 cm^{-1} of electrolytes.

a temperature range of −70 to +70 °C are evaluated (Figure S1, Figure 2a, Figure S2). Figure S1a shows the cathodic scan of Zn || Ti half-cells at a scanning rate of 5 mV s^{-1} in 1.0 m and 7.6 m $ZnCl_2$ electrolytes. In 1.0 m $ZnCl_2$ electrolyte, water began to reduce at a potential of 0.36 V, followed by Zn deposition at a potential of −0.022 V. However, in 7.6 m $ZnCl_2$ electrolyte, the water reduction is largely suppressed as evidenced by the significantly reduced water-reduction current due to formation of zincophilic-zincophobic SEI. The zincophilic-zincophobic SEI only shift the Zn plating potential from 22 mV in 1.0 m to 28 mV in 7.6 m $ZnCl_2$. During anodic scan (Figure S1b), the oxygen evolution reaction onset potential increases from 2.0 V in 1 m $ZnCl_2$ to 2.3 V in 7.6 m $ZnCl_2$. The enlarged electrochemical stability allows the electrolyte to support high voltage cathodes, effectively increasing energy density of batteries. In addition to the stability window, the ionic conductivity of electrolytes with concentration range from 1 m to 30 m $ZnCl_2$ was evaluated. 7.6 m $ZnCl_2$ electrolyte delivers the highest ionic conductivity from −70 to 70 °C (Figure S2), which is consistent with Chen's findings.[2] At a low temperature of −70 °C, the 7.6 m $ZnCl_2$ electrolyte still shows remarkable conductivity of

0.76 mS cm^{-1}, which is 76 and 760 times higher than those of 1 m and 30 m $ZnCl_2$ respectively, since $ZnCl_2$-H_2O is in an eutectic at 7.6 m with glass transition temperature (T_0) of 155 K, while the glass transition temperatures of 1 m and 30 m $ZnCl_2$ electrolytes are 173 and 189 K, respectively, which are higher than that of 7.6 m $ZnCl_2$ (Figure S3, Table S1, Note S1).

To understand the electrolyte structure of 7.6 m and 1 electrolytes, X-ray absorption spectroscopy (XAS) was performed. In XAS, the edge position (when the normalized absorption coefficient is 0.5) in the X-ray absorption near edge structure (XANES) spectra of Zn is a good indicator of the effective charge on Zn. Figure 2b shows that 1 m and 7.6 m $ZnCl_2$ have different edge energies, suggesting that Zn^{2+} have different solvation structures. The dominant electronegative elements (O in H_2O as in 1 m $ZnCl_2$, Cl^- anion as in 7.6 m $ZnCl_2$) in the solvation structure attract electrons around Zn^{2+}, leading to decreased electron density around Zn^{2+}. Zn spectrum of 7.6 m $ZnCl_2$ with lower average edge energy indicates there are more electrons around Zn^{2+} due to lessened charge transfer from Zn^{2+} to the coordinating atom. One possibility is the replacement of O (as in H_2O) by Cl which is less electronegative. The Fourier transformed extended X-ray absorption fine structure (ft-EXAFS) in Figure 2c indicates that the ordered domain in these electrolytes are limited to the first shell, corresponding to the first and the strongest peak. The peak obviously shifts from 1 m to 7.6 m $ZnCl_2$, suggesting the presence of Cl^- in the first solvent shell as the Zn–Cl bond length ($\approx$2.3 Å in the $ZnCl_2$ crystal) is considerably longer than that of the Zn–O bond ($\approx$2.0 Å in $Zn(OH)_2$ crystal). As a result, the solvation shell of the 7.6 m $ZnCl_2$ is less compact, and the Zn^{2+} desolvation penalty and the solvated H_2O reduction are inhibited at the electrolyte-electrode interface during Zn plating/stripping, beneficial for reversible Zn anode.

The perturbations of water structure by salts was analyzed using Nuclear magnetic resonance (NMR).[11] The ^{67}Zn NMR spectroscopy demonstrated that Cl^- participates in Zn^{2+} solvation sheath. As in Figure 2d, the more positive ^{67}Zn chemical shift (144 ppm) in 7.6 m $ZnCl_2$ electrolyte than that (70 ppm) in 1 m $ZnCl_2$ indicates the deshielding effect on the Zn^{2+} solvation sheath with increased salt concentration (Figure S4, Note S2). This is consistent with the decreased electron density around Zn^{2+} and the increased Zn–O bond length (Figure 2b,c), leading to decreased Zn–O bond strength and reduced Zn^{2+} desolvation penalty.

The solvation species around Zn^{2+} was characterized using Raman spectrum. Figure 2e and Figure S5 show the stretching vibration type alteration for $[Zn(H_2O)_2Cl_4]^{2-}$, $[Zn(H_2O)_6]^{2+}$ and $[ZnCl_4]^{2-}$ with different $ZnCl_2$ molar fractions. As the $ZnCl_2$ concentration increases from 1 m to 4 m, Zn^{2+} ions are solvated by either of H_2O or Cl as $[Zn(H_2O)_2Cl_4]^{2-}$ and $[Zn(H_2O)_6]^{2+}$. In the 7.6 m $ZnCl_2$, the $[Zn(H_2O)_2Cl_4]^{2-}$ and polymeric species dominate, indicating the diminishment of free water and the extensive disruption of water network. When the $ZnCl_2$ concentration continuously increases from 7 m to 30 m, the $[Zn(H_2O)_2Cl_4]^{2-}$ and polymeric species appear successively, which are beneficial for reducing the reactivity of H_2O. However, for all these electrolytes, the presence of solvated water in $[Zn(H_2O)_6]^{2+}$ makes H_2O reduction unavoidable during Zn deposition. Additionally, the disruption of the water network by 7.6 m $ZnCl_2$ is confirmed by the wavenumber shift of the O-H spectral band, compared with those in pure water and 1 m $ZnCl_2$ (Figure 2f, Figure S6, Note S2). The disappearance of free water and disruption of hydrogen bonding reduce the reactivity of H_2O, beneficial for increased zinc plating/stripping efficiency. However, the presence of solvated water around the Zn^{2+} are still vulnerable for decomposition during Zn plating/stripping. Therefore, to further suppress water reduction, a robust SEI is necessary to kinetically protect water from being reduced.

Zn plating/striping in 7.6 m $ZnCl_2$-0.05 m $SnCl_2$ electrolyte

The low water activity and disrupted water hydrogen network in 7.6 m $ZnCl_2$ aqueous electrolytes suppresses water decomposition and enables operation of Zn batteries at a low temperature, as demonstrated by previous work.[2] To achieve a high cycling stability with a low overpotential, a zincophilic substrate for uniform Zn plating and a zincophobic SEI for Zn dendrite suppression should be in situ formed in the electrolyte during Zn plating/striping. To form such zincophilic/zincophobic bi-layer, we add 0.05 m $SnCl_2$ into 7.6 m $ZnCl_2$, where Sn plates on current collector prior Zn plating due to a high Sn deposition potential of 0.62 V vs. Zn/Zn^+. The deposited Sn is zincophilic, and serves as a nuclei site for uniform Zn plating[13] In addition, Sn suppresses H_2 evolution due to high H_2 evolution overpotential on Sn, promoting the followed formation of zincophobic $Zn_5(OH)_8Cl_2{\cdot}H_2O$ layer on top of Sn. The formed zincophobic $Zn_5(OH)_8Cl_2{\cdot}H_2O$ can suppress Zn dendrite growth.

The Zn plating/stripping stability in Zn || Zn symmetric cells and CE in Zn || Ti asymmetric cells were evaluated using 7.6 m $ZnCl_2$ electrolytes with and without $SnCl_2$ additive. In the cyclic voltammetry (CV) (Figure 3a), the onset potential at 0.37 V vs. Zn^{2+}/Zn in 7.6 m $ZnCl_2$-0.05 m $SnCl_2$ electrolyte, which is 34 mV positive than that of 1 m $ZnCl_2$, indicates Sn deposited before Zn electrodeposition, consistent with the positive potential (−0.14 V vs. standard hydrogen electrode, SHE) of Sn^{2+}/Sn than that (−0.76 V vs. SHE) of Zn^{2+}/Zn. The uniform Sn metal deposition on inert Ti current collector in Zn || Ti cell using 7.6 m $ZnCl_2$-0.05 m $SnCl_2$ electrolyte was confirmed by SEM-EDS mapping (Figure S7). The X-ray diffraction (XRD) was used to analyze the composition of cycled Zn electrode recovered from 7.6 m $ZnCl_2$-0.05 m $SnCl_2$ (Figure 3b). Sn deposition on Zn was confirmed by XRD. The pre-deposited smooth Sn layer provides strong adsorption to Zn,[8] contributing to uniform Zn plating and dense SEI formation. The zincophilic nature of Sn layer decreased overpotential by 34 mV (Figure 3a), beneficial for homogeneous Zn deposition and hydrogen evolution inhibition.

At a challenging low temperature of −40 °C, the Zn/Ti cell using 7.6 m $ZnCl_2$-0.05 m $SnCl_2$ shows nine times higher of zinc plating/stripping peak current than that using 1 m $ZnCl_2$ (Figure S8). When the temperature further decreases to −50 °C, the zinc plating/stripping still shows a peak current

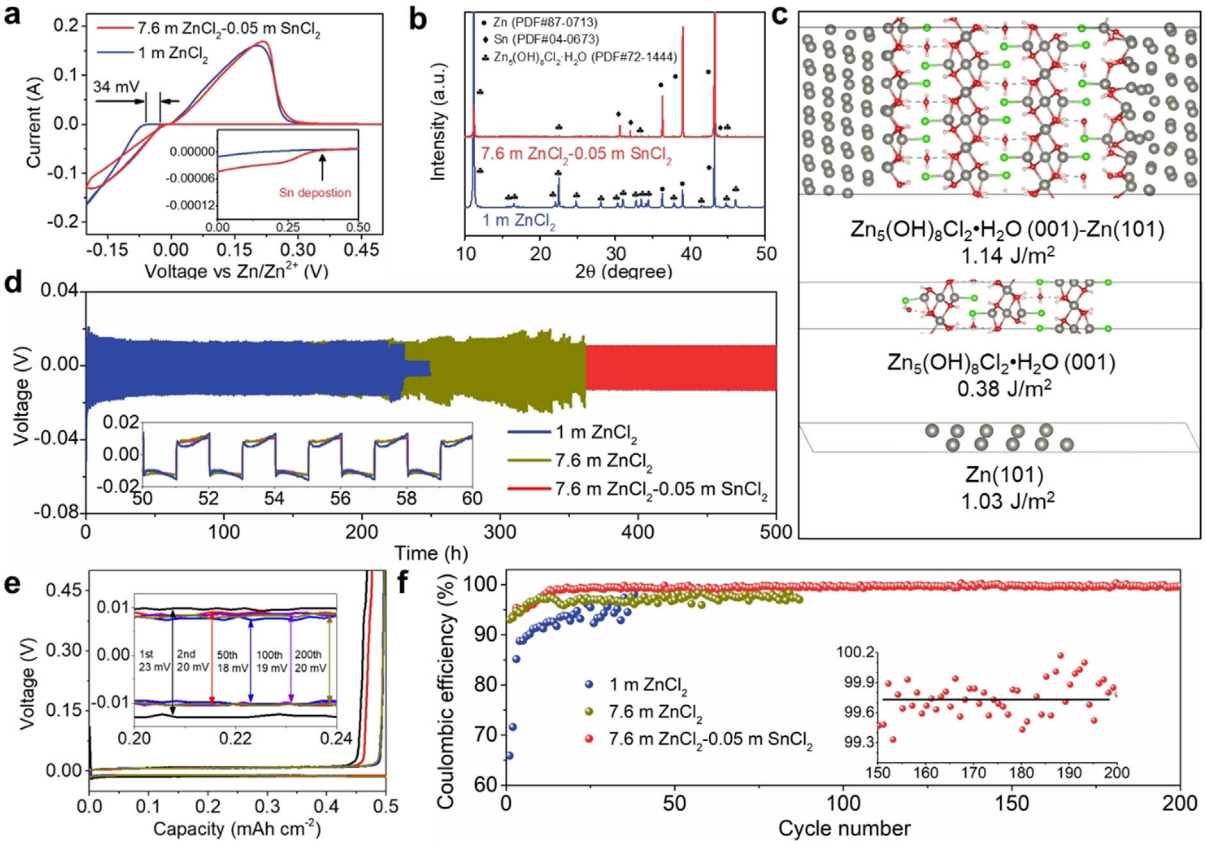

Figure 3. a) Cyclic voltammetry (CV) of titanium (Ti) working electrodes at a scan rate of 5 mV s^{-1} in $ZnCl_2$ electrolytes obtained in three-electrode cells with Ag/AgCl as reference electrode and Zn as a counter electrode. The potentials were converted to correspond to a Zn/Zn^{2+} reference. b) X-ray diffraction (XRD) spectra of cycled Zn in Zn || Ti cells in 1 m $ZnCl_2$ and 7.6 m $ZnCl_2$-0.05 m $SnCl_2$ electrolytes. c) Atomic structures and related surface/interfacial energies of $Zn_5(OH)_8Cl_2{\cdot}H_2O$ surface, Zn surface, $Zn_5(OH)_8Cl_2{\cdot}H_2O(001)$ | Zn(101) interface. d) Galvanostatic Zn plating/stripping in Zn || Zn cells at a current density of 3 mA cm^{-2} and a capacity of 3 mAh cm^{-2}. e) The charge/discharge curves of Zn plating/stripping processes at selected cycles in 7.6 m $ZnCl_2$-0.05 m $SnCl_2$ electrolyte at 1 mA cm^{-2}. f) Coulombic efficiency (CE) of Zn plating/stripping in Zn || Ti cells at 1 mA cm^{-2} and 0.5 mAh cm^{-2}.

in 7.6 m $ZnCl_2$-0.05 m $SnCl_2$, while the current in 1 m $ZnCl_2$ is almost ignorable. In addition to deposited Sn, XRD showed the formation of $Zn_5(OH)_8Cl_2{\cdot}H_2O$ on cycled Zn. The high zincophobicity of $Zn_5(OH)_8Cl_2{\cdot}H_2O$ was confirmed by surface energies of $Zn_5(OH)_8Cl_2{\cdot}H_2O(001)$ and Zn(101), and interface energy between them using density functional theory (DFT) (Figure 3c, Figure S9). The surface energy of $Zn_5(OH)_8Cl_2{\cdot}H_2O(001)$ and Zn(101) are 1.03 J m^{-2} ($\gamma Zn_5(OH)_8Cl_2{\cdot}H_2O$) and 0.38 J m^{-2} ($\gamma$Zn), respectively. The interfacial energy of $Zn_5(OH)_8Cl_2{\cdot}H_2O(001)$ | Zn(101) is 1.14 J m^{-2} ($\gamma Zn_5(OH)_8Cl_2{\cdot}H_2O$.Zn). According to the Young's equation, the contact angle (θ) is about 137°, indicating the zincophobic nature of basic $Zn_5(OH)_8Cl_2{\cdot}H_2O$ and effectively suppressing Zn dendrite.[14]

The zincophilic Sn and zincophobic $Zn_5(OH)_8Cl_2{\cdot}H_2O$ SEI can reduce Zn plating/stripping overpotential and suppress Zn dendrite growth. The stability of Zn anodes in 1 m $ZnCl_2$, 7.6 m $ZnCl_2$, and 7.6 m $ZnCl_2$-0.05 m $SnCl_2$ electrolytes were evaluated at 3 mA cm^{-2} and 3 mAh cm^{-2} using Zn || Zn cells. In Figure 3d, the Zn || Zn cell using 7.6 m $ZnCl_2$-0.05 m $SnCl_2$ electrolyte exhibits steady charge/discharge over 500 h, while that in the 1 m $ZnCl_2$ reference electrolyte shorts after only 220 h, and that using the 7.6 m $ZnCl_2$ reference electrolyte shows fluctuated overpotential after 250 h and shorts after 350 h. Even at ultra-low temperature of −70 °C, the Zn electrode still shows a high reversibility in 7.6 m $ZnCl_2$-0.05 m $SnCl_2$ in Zn || Zn cells (Figure S10). In addition, the zincophilic-zincophobic interface does not increase overpotential of Zn || Zn cells, as evidenced by similar overpotential of only ≈ 8 mV in all three electrolytes (Figure 3d). The reaction kinetics of Zn anodes in different electrolytes at room temperature were also compared in a high current densities of 10 mA cm^{-2}. As shown in Figure S11, at both capacities of 3 and 10 mAh cm^{-2}, the Zn || Zn cell using 7.6 m $ZnCl_2$-0.05 m $SnCl_2$ electrolyte shows smaller polarization as in 1 m $ZnCl_2$ electrolyte, but Zn || Zn cell in 7.6 m $ZnCl_2$-0.05 m $SnCl_2$ shows a longer cycle stability than that in 1 m $ZnCl_2$.

Furthermore, the Zn plating/stripping CE in different electrolytes were compared using Zn || Ti cells at a current of 1 mA cm^{-2} and a capacity of 0.5 mAh cm^{-2}. As displayed in Figure 3e,f, the cells using 7.6 m $ZnCl_2$-0.05 m $SnCl_2$ demonstrates a low overpotential of ≈ 20 mV and a high CE of 99.7 % for 200 cycles (Figure 3f). To sharp contrast, the Zn || Ti cell using 1 m $ZnCl_2$ shows fluctuant voltage profiles with a low CE of ≈ 92.0 % and short circuit after only ≈ 20 cycles.

Under identical conditions, the Zn || Ti cell using 7.6 m $ZnCl_2$ electrolyte shows fluctuant voltage signals with a CE of ≈97.0% and is short-circuit after only ≈87 plating/stripping cycles. Therefore, the high reversibility of Zn plating/stripping in 7.6 m $ZnCl_2$-0.05 m $SnCl_2$ comes from formation of zincophilic Sn and zincophobic $Zn_5(OH)_8Cl_2{\cdot}H_2O$ SEI. Additionally, the initial potential before discharge in Figure 3e is attributed to the electro-deposition of Sn metal, consistent with the onset potential of 0.37 V vs. Zn^{2+}/Zn for Sn deposition (Figure 3a).

The surface morphologies of Zn electrode after plating/stripping are characterized using scanning electron microscope (SEM). After 50 cycles, the Zn cycled in 1 m $ZnCl_2$ become porous with thickness of 14.8um due to formation of flake-like dendrites (Figure 4a–c), as evidenced by a low CE

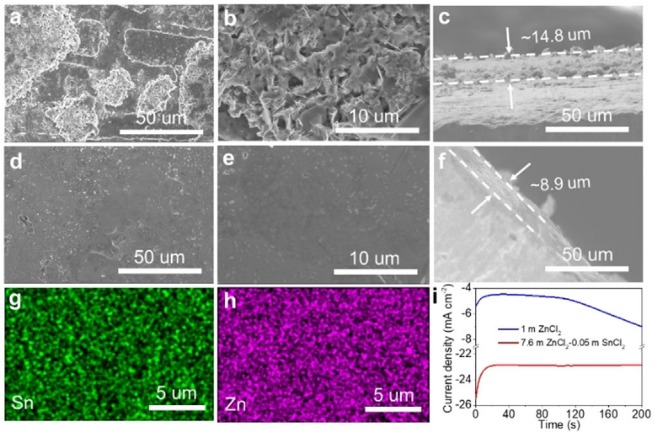

Figure 4. Scanning electron microscope (SEM) images of Zn electrodes in Zn || Zn cells after 50 plating/stripping cycles at 1 mA cm^{-2} and 1 mAh cm^{-2} in a)–c) 1 m $ZnCl_2$ and d)–f) 7.6 m $ZnCl_2$-0.05 m $SnCl_2$ electrolytes. In (c) and (f), broken white lines indicated the etching depth in cross-section view. g),h) The energy dispersive spectroscopy (EDS) mapping of the Zn recovered from 7.6 m $ZnCl_2$-0.05 m $SnCl_2$ electrolyte. i) Chronoamperograms (CAs) of Zn electrodes at an overpotential of −50 mV.

(≈92%) and poor cycling stability. When the $ZnCl_2$ concentration increased to 7.6 m, the Zn electrode still shows a porous surface morphologies (Figure S12, Figure S13) due to the absence of dense SEI. In sharp contrast, the Zn cycled in 7.6 m $ZnCl_2$-0.05 m $SnCl_2$ exhibits a dense and thin (8.9 μm) dendrite-free morphology (Figure 4d–f, Figure S12), confirmed by the uniform Zn, Sn and Cl elements distribution (Figure 4g,h). The reduction of cycled Zn thickness from 14.8 μm in 1 m $ZnCl_2$ to 8.9 μm in 7.6 m $ZnCl_2$-0.05 m $SnCl_2$ (white lines in Figure 4c,f), further confirmed the effective Zn dendrite suppression in 7.6 m $ZnCl_2$-0.05 m $SnCl_2$ electrolyte. Therefore, 7.6 m $ZnCl_2$-0.05 m $SnCl_2$ electrolyte effectively suppresses water reaction with Zn anode and dendritic growth due to the decreased water activity, formation of zincophilic Sn bottom sublayer and dense zincophobic-hydrophobic $Zn_5(OH)_8Cl_2{\cdot}H_2O$ top sublayer (Figure S14). To further scrutinize the deposited Zn film growth mechanism, chronoamperometry (CA) measurements were conducted. The variation in current versus time at a constant potential can sensitively reflect the nucleation process and surface change. In Figure 4i, for the Zn || Zn cell using 1 m $ZnCl_2$ electrolyte, the current density quickly increases after an overpotential of 50 mV is applied for 120 s, suggesting a rapid increase of effective surface area, as evidenced by the porous and rough plated Zn in Figure 4a,b. While in 7.6 m $ZnCl_2$-0.05 m $SnCl_2$, the current density remains constant, indicating that the dendritic growth was inhibited, consistent with the smooth electrode surface in Figure 4d,e.

$Zn_5(OH)_8Cl_2{\cdot}H_2O$ SEI formation mechanism

AIMD simulations were performed to further understand the formation mechanism for $Zn_5(OH)_8Cl_2{\cdot}H_2O$ SEI. The association of Zn^{2+}, OH^-, Cl^-, and H_2O species on the (0001) Zn surface were calculated. Representative snapshots are shown in Figure 5a–h, Figure S15 and Figure S16. The increased Zn^{2+}: OH^- ratio of approximate 5:8 at the metal-electrolyte interface triggers the formation of an interfacial

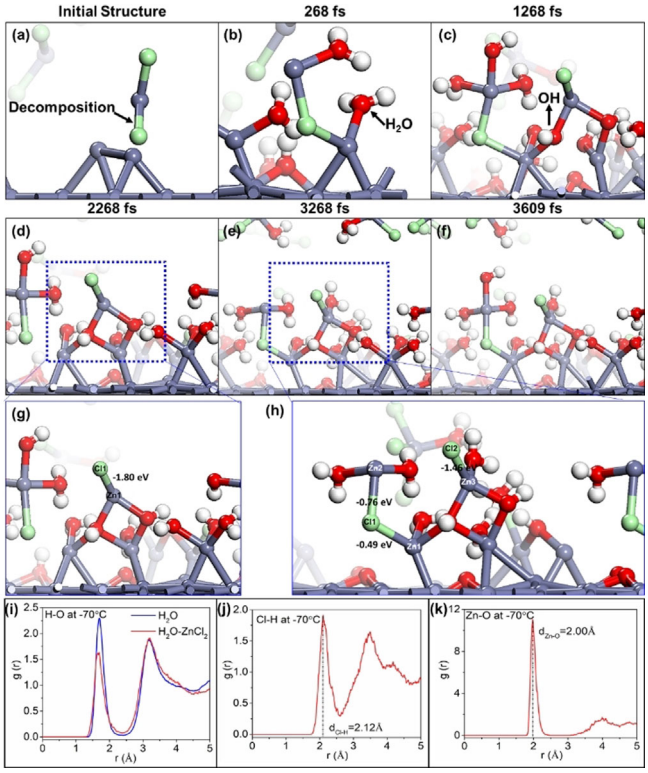

Figure 5. Evolution of interfacial structure made up of Zn^{2+}, OH^-, Cl^-, and H_2O species on the (0001)Zn surface. a) The initial adsorption of Zn^{2+} and nearby $ZnCl_2$ molecule. b) The formation of a Zn-Cl-Zn complex interacting with water molecules. c) Snapshot at 1268 fs revealing how OH^- molecules serve as a bridge connecting two Zn atoms. d)–f) The increased association of species on the (0001)Zn surface within the first 4 ps of simulation time. g),h) The ICOHP energy strength value (in eV) of selected Zn–Cl bonds. Color code: Red O, white H, green Cl and dark grey spheres Zn. i) H-O radial distribution functions of pure water and water in 7.6 m $ZnCl_2$ calculated from AIMD simulations at −70°C. j) Cl-H and k) Zn-O radial distribution functions of interactions between $ZnCl_2$ and H_2O in 7.6 m $ZnCl_2$ at −70°C.

structure on the surface of the (0001) Zn slab. In detail, the initial formation of the interfacial structure starts with the deposition of Zn^{2+} on the (0001) Zn surface (Figure 5a) and the rapid dissociation of a nearby $ZnCl_2$ molecule. At approximately 268 fs, the dissociated $ZnCl_2$ molecule (i.e., ZnCl) interacts with an adsorbed Zn to create a Zn-Cl-Zn complex. Simultaneously, water molecules solvate this newly formed Zn-Cl-Zn complex (Figure 5b). Besides, within the first few picoseconds of simulation time, some OH^- molecules adsorbed on the (0001) Zn surface and others also act as a bridge between nearby Zn atoms (Figure 5c).

To provide insight into the nature of bonding interactions between the species in this interfacial structure, we estimated the bond strength between relevant species where bonding is expected to occur based upon the trajectories of the simulation. The bond strength analysis indicates that the nature of the Zn–Cl bond for the configuration in Figure 5d–f is covalent and ranges between −0.49 and −1.80 eV (Figure 5g,h). Thus, the Zn-Cl is covalent (very strong) in some cases and the trend is more likely to continue during system evolution. Indeed, snapshots taken of the system evolution up to 10 ps of simulation time continue to display the increased association of species on the (0001) Zn surface. Therefore, based on the species involved, their dynamics and bonding interactions, we speculate that the interfacial structure is a precursor of the $Zn_5(OH)_8Cl_2\ H_2O$ structure.

Moreover, we investigated the hydrogen bond network of water in this electrolyte solution model in the presence of the (0001) Zn surface with the local concentration of Zn^{2+} and OH^-. Hydrogen bonds are highly dynamic in nature, and keep forming and breaking over the course of the AIMD simulation. Therefore, for the (0001) Zn slab model, we computed the average number of hydrogen bonding per molecule containing an oxygen atom (Figure S17). The analysis reveals that a sharp decline of the H-bonding network takes place within the first picosecond of simulation time and thereafter it plateaus around an average H-bonding of approximately 2.2 H-bonds per oxygen containing molecule. Furthermore, to remove the effect of the (0001) Zn surface, we evaluated pair radial distribution functions (rdfs) $g_{ij}(r)$ between atoms i and j in bulk pure water and 7.6 m $ZnCl_2$ bulk solutions at −70 °C to reveal the differences in water structure and number of H bonds due to the presence of the salt. Here, $g_{ij}(r)$ are dimensionless functions representing the ratio between the local density of atoms j located at a radial distance r from atom i, and the corresponding bulk density of atoms j in solution.[15] The H-O, O-O, and H-H rdfs (Figure 5i, Figure S18a,b) are descriptors for the interactions between water molecules in pure water and 7.6 m $ZnCl_2$. The first peak intensity of the g_{OH}, indicative of the number of H-bonds, is reduced from 2.26 in pure water to 1.59 in 7.6 m $ZnCl_2$. A second indicator is the depth in the minimum after the first peak that in the solution is slightly above the one for pure water indicating weakened H bonds.[16] Based on the integration of $g_{OH}(r)$, the number of H-bonds is reduced from 4 in pure water to 2.2 in 7.6 m $ZnCl_2$ at −70 °C. The number of H-bonds calculated in bulk agrees with the one obtained in water surrounding the surface. The reduced first peak position in the $g_{O\text{-}O}(r)$ (from 4.31 to 3.20) and the $g_{H\text{-}H}(r)$ (from 1.93 to 1.63), and the increased depth of the first minimum of $g_{O\text{-}O}(r)$ (from 0.28 to 0.78) confirmed the HB breaking effect of $ZnCl_2$ (Figure S18a,b).

Other features of the solution structure are observed in the rdfs between the salt and water atoms (Figure 5j–k, Figure S18c,d). The strong interactions between Cl and H_2O forms O-H···Cl^- hydrogen bonds. Figure 5j shows a well-defined first peak at ≈2.12 Å. Integrating the first peak of $g_{Cl\text{-}H}(r)$ reveals 2.5 H-bonds per Cl atom. The accompanying O atom in the water molecule is located at 3.1 Å (Figure S18c) as shown by the first peak of the $g_{Cl\text{-}O}(r)$. The $g_{Zn\text{-}O}(r)$ (Figure 5k) shows a very strong interaction of Zn with water. Note that the minimum after the first peak is almost zero, revealing a quasi-solid-state behavior of the water-Zn interaction. The number of water molecules surrounding the Zn atom are ≈3. The Zn–Cl bond (Figure S18d) remains sharp at its intramolecular distance (2.2 Å). The structural characteristics agree with the experimental EXAFS analysis in Figure 2.

Electrochemical performance of $VOPO_4$ || Zn full cells

The electrochemical performance of $VOPO_4$ || Zn full cells in 7.6 m $ZnCl_2$-0.05 m $SnCl_2$ and 1 m $ZnCl_2$ electrolytes was compared. In Figure 6a,b, at room temperature, the discharge capacities of $VOPO_4$ || Zn cells in both 1 m and 7.6 m $ZnCl_2$-0.05 m $SnCl_2$ electrolytes are about 163 mA g^{-1}. However, when the temperature is decreased to −50 °C, the $VOPO_4$ || Zn cell using 1 m $ZnCl_2$ electrolyte provide a low capacity of 23.1 mAh g^{-1}, while the $VOPO_4$ || Zn cell using 7.6 m $ZnCl_2$-0.05 m $SnCl_2$ can still provide a capacity of 105.7 mAh g^{-1} demonstrating the high redox reversibility and low-temperature tolerance of 7.6 m $ZnCl_2$-0.05 m $SnCl_2$ electrolyte. The rapid capacity decay of $VOPO_4$ || Zn cell in 1 m $ZnCl_2$ (Figure 6a) is because that the conductivity of 1 m

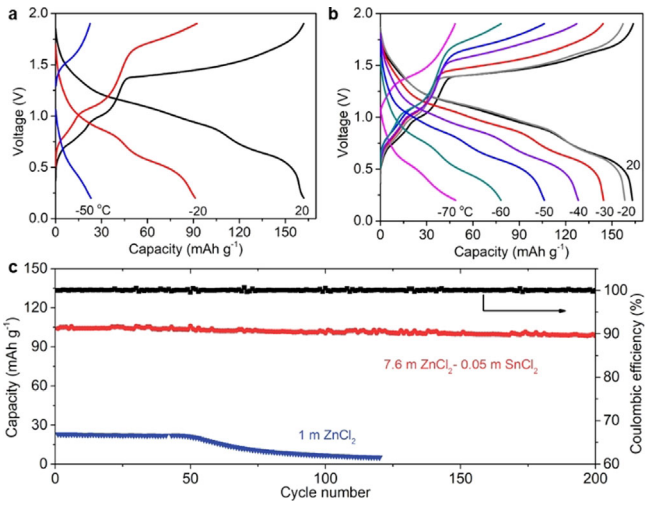

Figure 6. Electrochemical performance of $VOPO_4$ || Zn cells using different electrolytes at different temperatures. Charge/Discharge profiles of $VOPO_4$ || Zn cells using a) 1 m and b) 7.6 m $ZnCl_2$-0.05 m $SnCl_2$ electrolytes. c) Cycling performance of $VOPO_4$ || Zn cells using different electrolytes at −50 °C with a charge/discharge current density of 1/3 C.

$ZnCl_2$ decreases to only 0.3 mS cm^{-1} at −50 °C (Figure 2a, Figure S2). Furthermore, even when the temperature decreases to −70 °C, the $VOPO_4$ || Zn cell using 7.6 m $ZnCl_2$-0.05 m $SnCl_2$ can still deliver a capacity of 48.7 mAh g^{-1}. The $VOPO_4$ || Zn cell using 7.6 m $ZnCl_2$-0.05 m $SnCl_2$ also shows much longer cycling stability than that in 1 m $ZnCl_2$ at −50 °C and 1/3 C rate. As demonstrated in Figure 6c, at −50 °C, $VOPO_4$ || Zn cell using 7.6 m $ZnCl_2$-0.05 m $SnCl_2$ can maintain a high-capacity retention of > 95 % after 200 cycles, while $VOPO_4$ || Zn cell using 1 m $ZnCl_2$ loses its capacity rapidly in 100 cycles at −50 °C.

Conclusion

We introduced 0.05 m $SnCl_2$ additive into eutectic 7.6 m $ZnCl_2$ aqueous electrolyte to in situ form zincophilic-zincophobic interfacial layer on Zn anode. First, the bottom layer of zincophilic Sn tightly anchors the deposited Zn, suppresses H_2 evolution and facilitates the formation of a uniform zincophobic $Zn_5(OH)_8Cl_2$ H_2O SEI. Second, the top layer of zincophobic $Zn_5(OH)_8Cl_2$ H_2O SEI with a smooth morphology facilitates Zn^{2+} diffusion and suppresses Zn dendrites, ensuring a long-term Zn stripping/plating even at a high current density with a high Zn capacity. Third, the eutectic composition considerably decreases the melting point and increases the low temperature conductivity of aqueous electrolyte due to the optimized charge carrier density and mobility leveraging the high reversibility of Zn metal anode and high ionic conductivity of electrolyte. The eutectic 7.6 m $ZnCl_2$-0.05 m $SnCl_2$ electrolyte enabled the $VOPO_4$ || Zn full cell an excellent cycling performance in a wide temperature range from −70 to 20 °C.

Acknowledgements

C. Wang at the University of Maryland gratefully acknowledges funding support from the Advanced Research Projects Agency-Energy under Contract No. DEAR0000962. E. Hu, and X.-Q. Yang at Brookhaven National Laboratory (BNL) were supported by the Assistant Secretary for Energy Efficiency and Renewable Energy, Vehicle Technology Office of the U.S. Department of Energy through the Advanced Battery Materials Research (BMR) Program under contract DE-SC0012704. This research used beamlines 7-BM of the National Synchrotron Light Source II, a U.S. DOE Office of Science User Facility operated for the DOE Office of Science by Brookhaven National Laboratory under Contract No. DE-SC0012704. Supercomputer resources from the Texas A&M University High Performance Research Computing and Texas Advanced Computing Center (TACC) are gratefully acknowledged.

Conflict of Interest

The authors declare no conflict of interest.

Keywords: aqueous zinc batteries · hydrogen bonds · low temperature · salt precipitation · zincophilic–zincophobic interfacial bilayer

[1] F. Wang, O. Borodin, T. Gao, X. Fan, W. Sun, F. Han, A. Faraone, J. A. Dura, K. Xu, C. Wang, *Nat. Mater.* **2018**, *17*, 543–549.
[2] Q. Zhang, Y. Ma, Y. Lu, L. Li, F. Wan, K. Zhang, J. Chen, *Nat. Commun.* **2020**, *11*, 4463.
[3] C. Zhang, W. Shin, L. Zhu, C. Chen, J. C. Neuefeind, Y. Xu, S. I. Allec, C. Liu, Z. Wei, A. Daniyar, J.-X. Jiang, C. Fang, P. A. Greaney, X. Ji, *Carbon Energy* **2021**, 3, 339–348.
[4] X. Wu, Y. Xu, C. Zhang, D. P. Leonard, A. Markir, J. Lu, X. Ji, *J. Am. Chem. Soc.* **2019**, *141*, 6338–6344.
[5] a) L. Cao, D. Li, E. Hu, J. Xu, T. Deng, L. Ma, Y. Wang, X.-Q. Yang, C. Wang, *J. Am. Chem. Soc.* **2020**, *142*, 21404–21409; b) L. Cao, D. Li, T. Deng, Q. Li, C. Wang, *Angew. Chem. Int. Ed.* **2020**, *59*, 19292–19296; *Angew. Chem.* **2020**, *132*, 19454–19458.
[6] L. Kang, M. Cui, F. Jiang, Y. Gao, H. Luo, J. Liu, W. Liang, C. Zhi, *Adv. Energy Mater.* **2018**, *8*, 1801090.
[7] Z. Zhao, J. Zhao, Z. Hu, J. Li, J. Li, Y. Zhang, C. Wang, G. Cui, *Energy Environ. Sci.* **2019**, *12*, 1938–1949.
[8] Y. Yin, S. Wang, Q. Zhang, Y. Song, N. Chang, Y. Pan, H. Zhang, X. Li, *Adv. Mater.* **2020**, *32*, 1906803.
[9] J. Zheng, Q. Zhao, T. Tang, J. Yin, C. D. Quilty, G. D. Renderos, X. Liu, Y. Deng, L. Wang, D. C. Bock, C. Jaye, D. Zhang, E. S. Takeuchi, K. J. Takeuchi, A. C. Marschilok, L. A. Archer, *Science* **2019**, *366*, 645–648.
[10] Y. Marcus, *ACS Sustainable Chem. Eng.* **2017**, *5*, 11780–11787.
[11] T. DeFries, J. Jonas, *J. Chem. Phys.* **1977**, *66*, 896–901.
[12] C. Zhang, J. Holoubek, X. Wu, A. Daniyar, L. Zhu, C. Chen, D. P. Leonard, I. A. Rodríguez-Pérez, J.-X. Jiang, C. Fang, X. Ji, *Chem. Commun.* **2018**, *54*, 14097–14099.
[13] S. Li, J. Fu, G. Miao, S. Wang, W. Zhao, Z. Wu, Y. Zhang, X. Yang, *Adv. Mater.* **2021**, *33*, 2008424.
[14] L. Cao, D. Li, T. Pollard, T. Deng, B. Zhang, C. Yang, L. Chen, J. Vatamanu, E. Hu, M. J. Hourwitz, L. Ma, M. Ding, Q. Li, S. Hou, K. Gaskell, J. T. Fourkas, X.-Q. Yang, K. Xu, O. Borodin, C. Wang, *Nat. Nanotechnol.* **2021**, DOI: 10.1038/s41565-021-00905-4.
[15] M. P. Allen, D. J. Tildesley, *Computer simulation of liquids*, Oxford University Press, Oxford, **2017**.
[16] E. Guardia, I. Skarmoutsos, M. Masia, *J. Phys. Chem. B* **2015**, *119*, 8926–8938.

Manuscript received: June 2, 2021
Accepted manuscript online: July 1, 2021
Version of record online: ■■ ■■, ■■■■

Research Articles

Zinc Batteries

L. Cao, D. Li, F. A. Soto, V. Ponce, B. Zhang, L. Ma, T. Deng, J. M. Seminario, E. Hu, X. Yang, P. B. Balbuena,* C. Wang* ——— ▮▮▮▮–▮▮▮▮

Highly Reversible Aqueous Zinc Batteries enabled by Zincophilic–Zincophobic Interfacial Layers and Interrupted Hydrogen-Bond Electrolytes

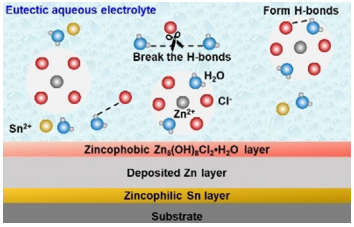

A highly reversible Zn anode working at low temperature is achieved by introducing $SnCl_2$ into eutectic $ZnCl_2$ aqueous electrolyte to form a zincophilic–zincophobic interfacial layer on the Zn anode in situ. The bottom layer of Sn facilitates uniform Zn deposition, while the top layer of zincophobic $Zn_5(OH)_8Cl_2$ H_2O facilitates Zn^{2+} diffusion and avoid Zn dendrites. The eutectic composition enhances the low temperature conductivity.